Final Report

Department of Energy

Office of Basic Energy Sciences

Award No. DE-FG0207ER46464

Title of Award:

Luminescence in Conjugated Molecular Materials under Sub-bandgap Excitation

Principal Investigator

Franky So
Professor
University of Florida
Department of Materials Science and Engineering
P. O. Box 116400
Gainesville, FL 32611-6400
Phone: (352) 846-3790
Fax: (352) 846-1182
E-mail: fso@mse.ufl.edu

Final Report

(May 8, 2014)

Period: Sept 1, 2010 – December 31, 2013

Achievements

The objective of our recent DOE effort has been to study sub-bandgap electroluminescence using ZnO nanoparticles (NPs) as an electron transport layer. We found that when the polymer/NPs interface form a type-II heterojunction and hole transporting polymers such as MEH-PPV and MDMO-PPV, luminance was observed when a sub-bandgap voltage was applied to the device. When electron transport polymers were used, sub-bandgap electroluminescence was not observed. In addition to polymer light emitting diodes, we have also observed sub-bandgap electroluminescence in small molecule devices using rubrene as an emitter and fullerene as an electron transport layer. Previously, we used the Auger model to explain the luminescence at voltages below the bandgap voltages. With our recent data, we attribute the sub-bandgap EL is due to triplet-triplet annihilation (TTA) in rubrene originated from the formation of charge transfer excitons. Transient EL decay of sub-bandgap emission shows the characteristic of TTA. The presence of charge transfer states in this system is verified with electroabsorption measurements. Our transient photoluminescence decay measurements further prove the increase of triplet density is coming from the charge transfer states. During the course of this research project, we have found interesting defect properties of ZnO NPs. We discovered that the defects present in ZnO NPs leads to strong interface carrier recombination. By treating ZnO NPs films with UV ozone, we observed that most of the dangling bonds are passivated, resulting in a significant reduction in interface recombination when these films are used as an electron transporting layer in a solar cell. Including the manuscripts submitted and under review, we have 10 publications during this period, with one paper published in *Nature Photonics*, one paper in *Advanced Energy Materials*, two papers in *Advanced Functional Materials*, one paper submitted to *Nature Communications* under review, and one paper to be submitted to *Advanced Energy Materials*. In addition to the systematic study of sub-bandgap luminescence, we have also developed a novel technique -- charge modulation electroabsorption spectroscopy to directly measure the effective bandgap energies of organic donor-acceptor systems for the first time. This technique will be used for the current proposed work to study the energetics in polymer solar cells and correlate the results with their dielectric properties. We do not anticipate any unexpended funds that will remain at the end of the current project period. Below are the highlights of some of our achievements.

1 Study of origin of sub-bandgap electroluminescence

In addition to the MEHPPV system which we observed sub-bandgap EL previously, another sub-bandgap emission systems is 5,6,11,12-Tetraphenylnaphthacene (rubrene)/fullerene bilayer structure[2]. Both rubrene and fullerene are widely studied semiconductors with high mobilities for holes and electrons, respectively. In the rubrene/fullerene heterostructure OLED, the device has an EL turn-on voltage of about 1 V which is about half the value of the rubrene bandgap (2.2 eV). The same EL spectrum of only rubrene emission observed below the bandgap voltage is the same as that above the bandgap. (Shown in Figure 1), indicating there is an up conversion process.

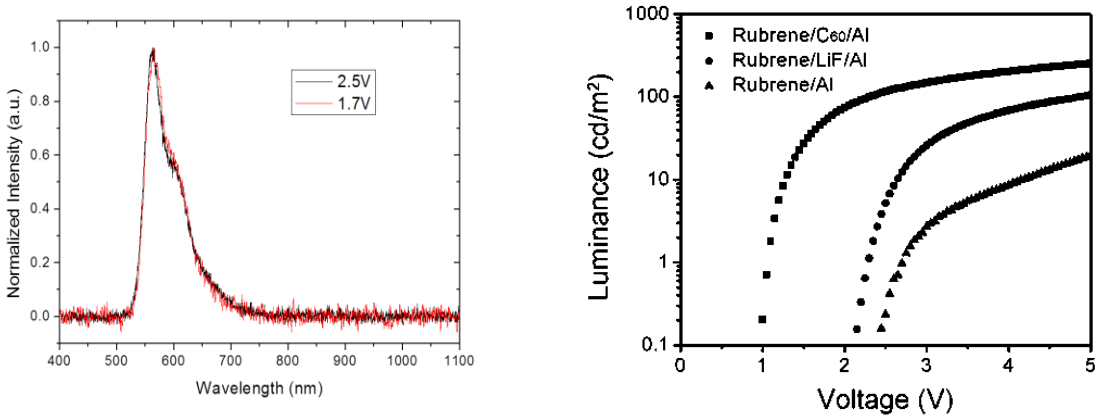

Figure 1. The EL spectra below and above band gap voltage (left) and L-V curves of rubrene OLEDs with different electron injecting layers (right).

Auger fountain mechanism has been proposed to explain this sub-bandgap phenomenon [1,2]. During the EL process in heterojunction devices, holes and electrons are injected from the rubrene and C_{60} layers, respectively. They recombine at the interface to give off energy to electrons at the LUMO level of C_{60}, which can overcome the energy barrier at the rubrene and C_{60} interface. After injected into the LUMO of rubrene, the Auger electrons recombine with holes in the HOMO and emits photons from rubrene[2-4]. However, even though near IR emission was observed in the planar heterojunction with a thin mixed layer between the rubrene and C_{60}, no evidence of Auger electron was reported.

Another possible up conversion phenomenon in rubrene is triplet-triplet annihilation (TTA)[5,6] where two triplets fused to form a singlet exciton. The triplet energy of rubrene is about half of its singlet state[7]. Therefore this kind of triplet fusion is more efficient in rubrene. A delayed fluorescent emission in rubrene was observed due to this process[5]. However, it turned out that in some systems, the amount of EL attributing to TTA substantially exceeds the limit imposed by spin statistics[8]. In this study, we investigated the charge transfer exciton using electroabsorpton spectroscopy, and showed from the transient EL measurement that delayed fluorescent emission dominating the EL of rubrene/C_{60} OLED. Finally, the increase of triplet density was observed with the present of rubrene/C_{60} heterojunction. All these observations indicate that the main mechanism of the sub-bandgap turn-on is the TTA stimulated by charge transfer excitons between rubrene and C_{60}.

To investigate the origin of the sub-bandgap EL phenomenon, we characterized the carrier transporting property using unipolar devices. The device structures are ITO/PEDOT(30nm)/Rubrene(60nm)/C_{60}(35nm)/Au and ITO/Rubrene(90nm)/C_{60}(35nm)/Al for hole and electron only devices respectively. The current density of the hole only device is more than two orders larger than that of the electron only device, indicating that holes are the dominating carriers in the device. Due to the large excessive hole carriers accumulated at the interface, a free electron that could play the role of 'Auger electron' is less likely to exist. Auger fountain mechanism is not suitable here.

TTA in the sub bandgap EL

If the sub-bandgap emission is due to TTA, delayed fluorescent EL emission is expected in the device. We conducted transient EL measurements on rubrene OLEDs with and without the C_{60} layer. The device structures are ITO/PEDOT/rubrene/Al and ITO/PEDOT/rubrene/C_{60}/Al. The rubrene only device has a luminance turn-on at 2 V, while the rubrene/C_{60} heterojunction device shows a low luminance turn-on at 1 V.

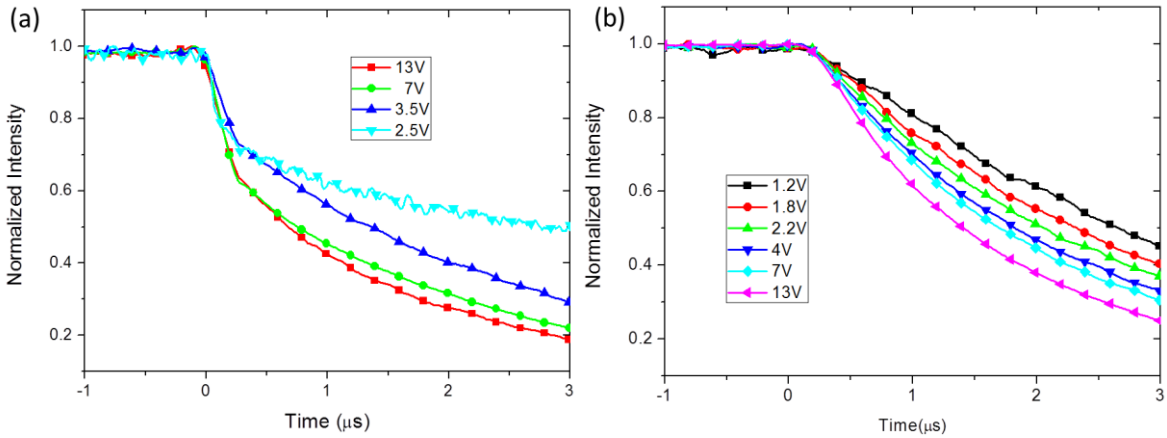

Figure 2. Transient EL decay of (a) rubrene OLED and (b) rubrene/C_{60} OLED

We first measured the EL transient decay at the trailing edge of a voltage pulse applied to the rubrene only device. The decay data are presented in Figure 2 (a). It is clear that there is a fast decay with a decay time less than 100 ns after voltage pulse following a long decay time in microseconds. Our data show the same TTA figure print decay curves as previous report[5]. The fast decay comes from the singlet excitons directly from the electron-hole recombination. With an increase in voltage, we observed a decrease of decay time of the delayed component. Long lived triplet is more easily quenched by injected polarons. When there is current injection, the rate equation of the triplet exciton density can be expressed as

$$\frac{d[T]}{dt} = -\frac{[T]}{\tau} - \gamma_{\mathrm{TT}}[T]^2 - k_{TP}[T][P],$$

where $[T]$ is the triplet density, τ is the triplet lifetime, $[P]$ is the polaron density, γ_{TT} is the TTA rate and k_{TP} is the triplet-polaron quenching (TPQ) rate. TPQ is not significant at low current density. Therefore if we only consider the first two terms in the equation at low current density, we obtained τ = 30±5 μs, which is in the same range as previous report[9]. In case of the rubrene/C_{60} heterojunction device, we also measured the EL decay at the trailing edge of the voltage pulse as shown in Figure 2 (b). Here, the fast decay component was not present and delayed fluorescent decay was observed for all applied voltages. With an increase in voltage, the decay time decreases as expected from the increase of TPQ. In the sub bandgap region, TTA is the only mechanism for the rubrene emission. We only consider the second term in the triplet time resolve equation, the triplet density is given as

$$[T] = \frac{[T_0]}{1 + \gamma_{\mathrm{TT}}[T_0]t}$$

The EL intensity which is resulted only from TTA is

$$I_{TTA} \sim \gamma_{TTA}[T]^2 \sim t^{-2}$$

Therefore, we expected the time resolved EL decay has a slope of -2 in logarithm plot. Figure 3 shows the fitting of EL decays driven in the sub bandgap region where TPQ is not significant. Both EL decays driven at 1.2 V and 1.8 V show a slope of -2, which indicates the TTA is the reason for the EL under the excitation of sub bandgap.

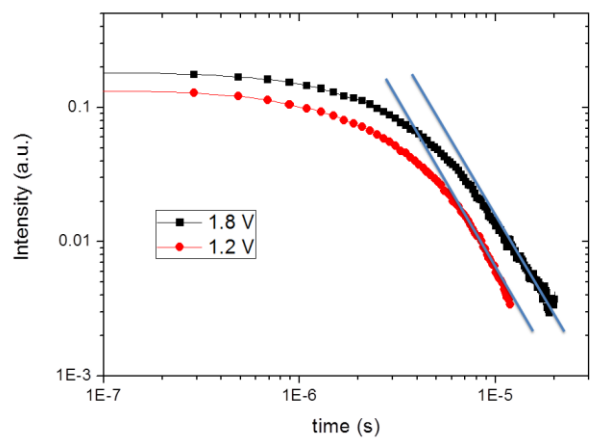

Figure 3. EL decay under sub-bandgap condition. Blue lines are fitting lines having slope of -2.

CT states at the rubrene/fullerene heterojunction

We attribute the formation of triplet excitons resulting in sub bandgap emission is due to the CT state formed at the rubrene/C_{60} interface. In order to prove the existence of the CT states, we measured the electroabsorption (EA) signal of pristine rubrene, pristine C_{60} and mix rubrene/C_{60} (2:1) blend. The quadrature signal from EA can distinguish the exciton and CT state due to slow response of the CT states to the AC electrical field[10]. Figure 4 shows the EA signal and its quadrature signal of the rubrene/C_{60} blend. There is an EA signal peaked at 1220 nm, which corresponds to the charge transfer state energy calculated from the energy band diagram. Its quadrature signal follows the EA signal. At wavelengths below 1150 nm, there is no quadrature signal. When the EA signal turns positive, the quadrature signal also starts and reaches a maximum value at 1220 nm. After the peak, both signals reduce. The negative signal of quadrature indicates the slow response to the AC electrical field. Therefore, the EA single at NIR region is from the CT states, which also agrees with the energy (1 eV) calculated from band diagram.

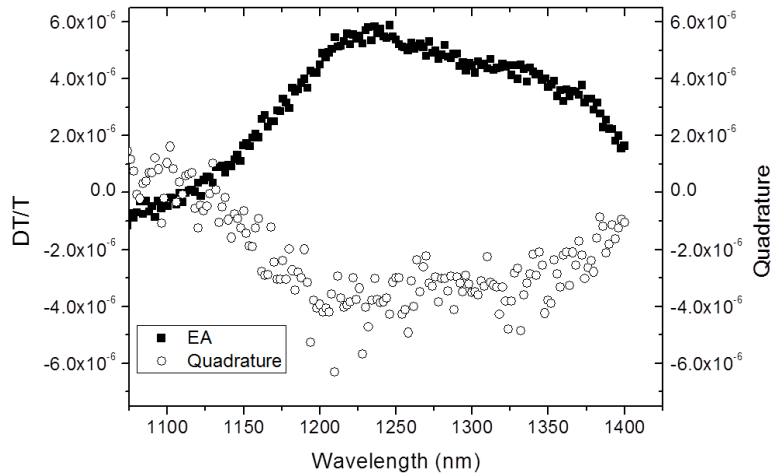

Figure 4. The in phase EA and its quadrature signals of the rubrene/C_{60} blend.

Energy transfer to triplets

We further conducted the transient PL measurements on the rubrene and rubrene/C_{60} blend (2:1) and measure the delay fluorescent decay component from rubrene emission, which is related to the triplet and charge transfer state. Rubrene also shows an efficient singlet fission process. Under high level excitation, significant amount of triplets can be generated which go through the triplet fusion process forming singlet exciton. As a result, a delayed fluorescent emission is also expected in PL measurement. Here we used a green pulse laser (527 nm) to excite the thin film. The excitation wavelength is overlap one of the absorption peak of rubrene. Figure 5 (a) shows the transient PL at shorter time (< 500 ns). The laser signal shows a good Gaussian shape with a Full width at Half Maximum (FWHM) of 10 ns, which is longer than the decay time of rubrene singlet. Therefore, there is no fast fluorescent component but only the delayed component in in both rubrene and rubrene/C_{60} blend. And the intensity of delayed component becomes larger in the rubrene/C_{60} blend. We show the PL decay in longer time scale and plot them in log-log scale in Figure 5 (b). These two lines are paralleled to each other over 3 orders of magnitude. Again as in the sub bandgap EL decay, this delayed fluorescent signal solely comes from the TTA with intensity proportional to the square of triplet density. Considering the first two terms in the time dependent differential equation, the time dependence of the triplet density is

$$[T] = \frac{[T_0]}{(1+[T_0]\gamma_{TT}\tau)e^{t/\tau} - [T_0]\gamma_{TT}\tau}$$

We fitted both decays according to $I_{TTA} \sim \gamma_{TTA}[T]^2$, and extracted the initial triplet density of them. Our fitting shows good agreement over 3-order of magnitudes in both films. And we found out (23±3) % times more triplets state in the rubrene/C_{60} blend than the pristine rubrene sample. Due to the large band offsets of HOMOs and LUMOs of rubrene and C_{60}, non-geminated recombination can be ruled out. Thus we attribute this increase of delayed rubrene fluorescent emission coming from the charge transfer states which created more initial triplet under photoexcitation.

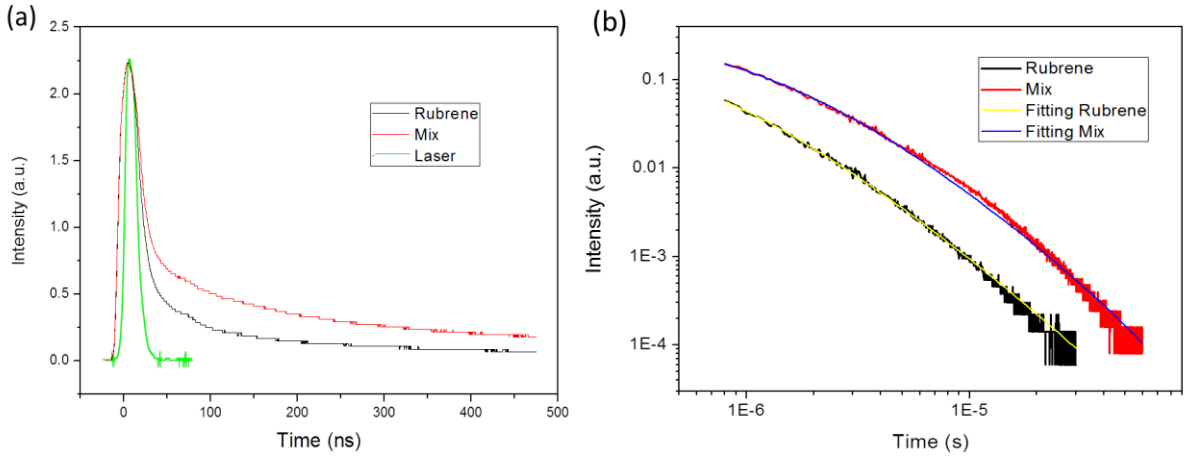

Figure 5. Transient PL of rubrene and rubrene/C_{60} below 500 ns (a) and over 500 ns (b).

Conclusion

We attribute TTA in rubrene is due to charge transfer excitons and produce the sub bandgap EL in rubrene/C_{60} heterojunction devices. The holes are the dominating carriers through this heterojunction, where free electrons are less likely to exist. Transient EL decay of sub bandgap emission shows the characteristic of TTA. Charge transfer states in this system is verified with EA measurements. Transient PL decay further proves the increase of triplet density is coming from the energy of charge transfer state.

2. Use of ZnO as electron extraction layer in photovoltaics cells

Colloidal ZnO nanoparticles are used as an electron extraction layer to fabricate inverted polymer solar cells. However, these nanoparticles are known to have a large density of defects and it has been shown that up to 30% of the atomic bonding in a ZnO nanoparticle are dangling bonds, resulting in a large density of recombination centers and low power conversion efficiencies (PCEs) in inverted polymer photovoltaic cells. It has been shown that a few seconds exposure of the device to ultraviolet (UV) light helps to temporarily fill the defect states in ZnO nanoparticles and results in enhanced device performance. Typically, this light soaking is done by exposing the device to a solar simulator and its effect lasts for a period of days with the device characteristics ultimately degrading over time. We demonstrated UV ozone (UVO) treated ZnO NP films immediately after processing can effectively passivate the defect states leading to longer carrier lifetimes in PV devices compared to devices treated only by light soaking. The resulting polymer PV devices with this treatment give enhanced short-circuit currents (J_{sc}) and fill factors (FF). Employing one specific high performance donor-acceptor (DA) copolymer, cells with power conversion efficiencies (PCEs) exceeding 8% are demonstrated.

The inverted cell used in this study has the following structure: ITO/ZnO NPs/ polymer: fullerene/molybdenum oxide (MoO_3)/silver. For the active layer materials, we used PDTG-TPD, and PDTS-TPD blended with $PC_{71}BM$. Our recently study on PDTG-TPD and PDTS-TPD inverted devices showed that a higher J_{sc} was obtained in PDTG-TPD containing devices compared to PDTS-TPD resulting in cells with up to 7.3% PCE. Using poly(vinyl pyrrolidone) (PVP) capped zinc oxide nanocomposites to form an electron transport layer, a 15% enhancement in PCE was achieved in the PDTG-TPD: $PC_{71}BM$ cells upon removal of the top surface layer of PVP from the nanoclusters by UV-ozone treatment prior to deposition of the active layer. Here, using pure colloidal ZnO NPs (Figure 6 (a)) without PVP composites as the electron transporting layer, we report a significant solar cell efficiency enhancement by reducing interfacial recombination via UV ozone treatment, resulting in solar cells with PCEs in excess of 8%.

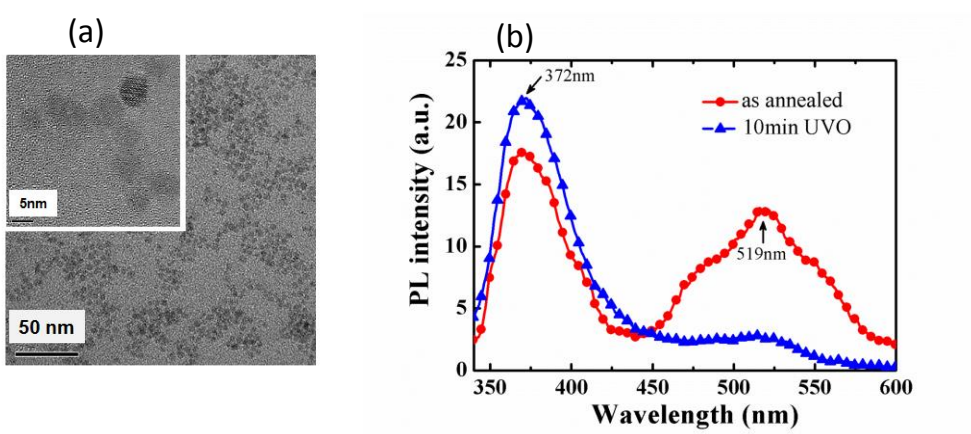

Figure 6: (a) Transmission electron microscopy (TEM) images of ZnO colloidal nanoparticles. (b) The steady state photoluminescence spectra of ZnO NPs films.

In order to passivate the ZnO NPs films used for the devices, the films were exposed to UV light at 254 nm for 10 minutes after first annealing at 80C. The passivation effect on ZnO NP films by this UVO treatment was investigated by photoluminescence measurements. As shown in

Figure 6 (b), in addition to the band-to-band emission of the ZnO NPs film at 372 nm, a strong broad emission band with a maximum at 519 nm was also observed for the untreated films and this emission band has been reported as an evidence of the presence of defect states[1,2]. Upon UVO treatment, however, this broadband defect emission is effectively quenched, indicating a significant reduction of defects states. As a result, due to the reduction of the defect states emission, the resulting band-to-band emission peaked at 372 nm peak increases in intensity as shown in Figure 6 (b). It should be also noted that the UVO treatment does not only treat the ZnO films surface, it also passivates the defects in the bulk due to the porosity of the ZnO NPs films, as the PL signal is coming from both bulk rather than just the surface. Based on the PL data, this defect passivation in ZnO NPs films should lead to reduction of carrier recombination at the ZnO/photoactive layer interface, and enhancement in the performance of the resulting PV cells.

The current density-voltage (J-V) characteristics of a PDTG-TPD cell are shown in Figure 7. Upon defect passivation of the ZnO electron transport layers, the PDTG-TPD cell experiences a significant enhancement of J_{sc}. The control PDTG-TPD:$PC_{71}BM$ cells with only light soaking treatment give an average J_{sc} of 12.9 mA/cm^2 while the UVO treated devices give an average value of 14.1 mA/cm^2. In addition, there is a slight enhancement in the fill factor resulting in the average power conversion efficiency of the treated PDTG-TPD cells increases from 7.4% to 8.1%. The external quantum efficiency (EQE) spectra for these cells are illustrated in Figure 7 (b). Integrating the EQE data of PDTG-TPD cell with the A.M. 1.5G spectrum gives a short-circuit current of 14.0 mA/cm^2 which is only 1% different from the value measured directly from the photo-J-V data. As shown by the EQE spectra in Figure 1.6 (b), a maximum value of 72% at 675 nm is observed for the PDTG-TPD cell and this value is especially high for inverted polymer PV cells.

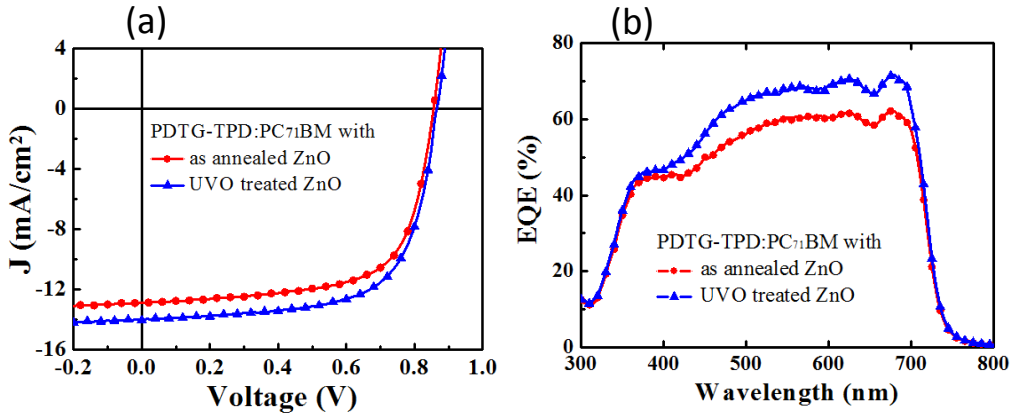

Figure 7: (a) J-V characteristics of PDTG-TPD: $PC_{71}BM$ and (b) EQE spectra of devices with and without UVO treatment.

The observed enhancements in J_{sc} and FF are consistent with the fact that the ZnO NPs are passivated due to the UVO treatment. To further confirm that the device enhancement is due to passivation of ZnO NPs, transient photo-current (TPC) measurements were carried out to study the photo-carrier decay dynamics under an extraction field. During the measurements, the active layer of the device was photo-excited by a pulsed laser with an emission power attenuated to ~10^2 nJ pulse^{-1} cm^{-2}, making sure the perturbation photocurrent < 0.1mA/cm^2, while the sample was also under a constant illumination from a solar simulator. Since the pulse laser source, which emits at 527 nm, does not excite the ZnO NPs, photo-generated carriers due to the laser pulse only come

from the polymer:fullerene blend. The single exponential decay of the transient photo-currents perturbation for the inverted cells with treated and untreated ZnO NPs films, as shown in Figure 1.9, is due to photo-generated carriers recombining either in the bulk or at the ZnO/photo-active layer interfaces. Determined from the photocurrent perturbation decay curves, the effective photo-carrier lifetimes are 130 ns and 210 ns for the untreated and UVO treated devices respectively, which is much shorter than the results generated by high level excitation TPC whose signals are dominated by carrier extraction. Since these devices have the same hole extraction contact and photo-active layer with identical transport properties, the difference in carrier lifetime must be attributed to carrier recombination at the ZnO/photo-active layer interface. Moreover, at short circuit condition, bulk recombination is unlikely to be the dominant loss mechanism and usually shows a lifetime longer than 10 μs since carriers are fairly depleted and extracted to the electrodes under an internal field ~ 10^5 V/cm. However, due to the existence of defects in the ZnO NPs, the photo-carriers excited by the laser pulse still recombine at a much faster rate via these mid-gap states at the ZnO/polymer interface. From the results of our transient photocurrent measurements, we conclude that defects are passivated by the UVO treatment which results in an increase both in carrier lifetime and photocurrent.

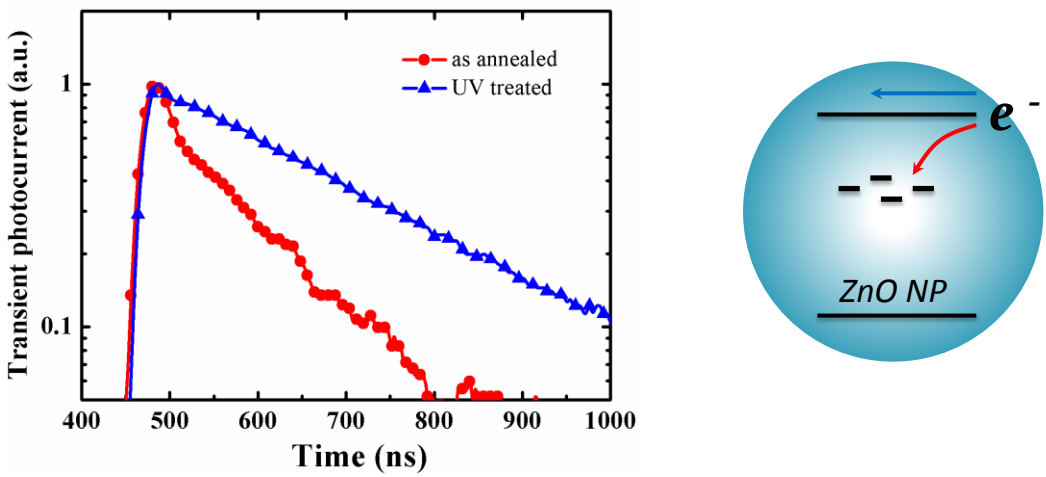

Figure 8: Transient photo-current decay for the inverted PDTG-TPD: $PC_{71}BM$ devices with "as annealed" and "UVO-treated" ZnO NPs films. The diagram on the right illustrates the recombination mechanism due to midgap states in ZnO NPs.

In summary, we reported a simple processing method to enhance the inverted PDTG-TPD: $PC_{71}BM$ PV cell efficiencies from 7.4% to 8.1%. The defects in ZnO films are passivated by UVO treatment, which is confirmed by the disappearance of defect emission in the photoluminescence spectrum and an increase in carrier lifetime determined from transient photo-current decay measurements. Similar effects were observed on PV cells based on PDTS-TPD. The EQE of the optimum cell reaches 72% at 675 nm, indicating that inverted PV cells based on PDTG-TPD are promising for photovoltaic applications and defects passivation treatment on ZnO NPs films can significantly enhance the device performance.

3. Use of electroabsorption spectroscopy to determine electron injection bariers

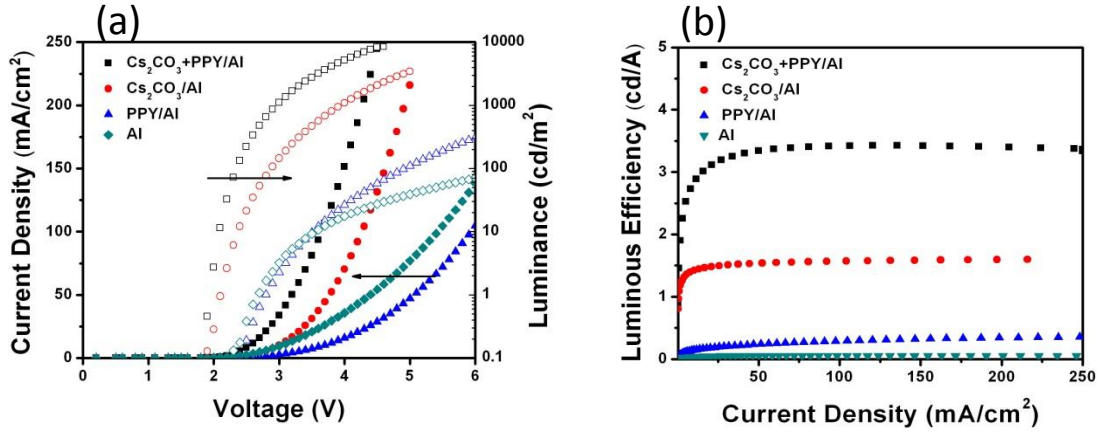

Figure 9. Luminance-Current-Voltage (L-I-V) characteristics for devices with varying interlayers (a) and Luminous efficiencies for devices with various interlayers (b).

Considerable efforts have been devoted to realize efficient electron injection through interfacial engineering such as modification of electrodes using thin films of alkaline metal fluorides such LiF and CsF. These occur by charge transfer between the interfacial polymer and metal contact as well as from the blocking of holes creating a local electric field which makes electron injection more facile. In this work, we explore a solution processed Cs_2CO_3 doped PPY polymer layer as a cathode interface layer to improve charge balance in MEH-PPV based polymer light emitting diodes (PLED). With the composite interface layer, a luminescence efficiency of 3.4 cd/A is demonstrated. Electroabsorption spectroscopy results indicate this is due to the low work function Cs_2CO_3 and favorable interface dipole which reduces the barrier for electron injection. The luminance-current-voltage (L-I-V) measurements were carried out for devices employing various cathode configurations and the results are summarized in Figure 9.

Given the fact that the barrier height of hole injection from PEDOT:PSS into MEH-PPV is small (0.1-0.2 eV) and MEH-PPV is a hole dominant polymer due to its higher mobility of holes than electrons, carrier recombination occurs near the cathode. With the addition of the PPY layer, holes are blocked at the MEH-PPV/PPY interface which yields a reduction in current density compared to the Al only cathode as seen in Figure 1.8(a). Although the device with Cs_2CO_3 shows higher current density due to its proven good electron injection abilities, the current density is further increased using the composite Cs_2CO_3 +PPY layer. The nitrogen atom of the pyridine side group of the PPY donates its electrons to the metal atoms in the electrode forming an interfacial dipole. This lifts the work function of the metal with respect to the LUMO level of the MEH-PPV and reduces the barrier for charge injection. As shown in Figure 1.8(a), the luminance value at 4.5 V for the PPY/Al cathode is 66 cd/m^2 compared to just 25 cd/m^2. This is due to the blocked holes at the EML/cathode interface recombining with injected electrons as well as more facile electron injection from the formation of the interface dipole. When Cs_2CO_3 is utilized to further enhance electron injection, the luminance value for the composite Cs_2CO_3 +PPY layer reaches 8412cd/m^2. This is much higher than using only Cs_2CO_3 interlayer which at 4.5V shows a luminance value of 2076cd/m^2.

Due to the blocked holes in the emission layer at the cathode interface as well as the presence of the interface dipole improving electron injection, the device efficiency improves from 0.02 cd/A for devices with the Al only cathode to 0.3 cd/A for devices with the PPY/Al cathode as shown in Figure 1.8(b). As expected, the Cs_2CO_3/Al cathode shows even better device

performance owing to the formation of a low workfunction contact and reaches a value of 1.6 cd/A. The current efficiency of the device with Cs_2CO_3 + PPY interlayer reaches 3.43 cd/A due to the further improvement in charge balance and is among the highest reported efficiencies for MEH-PPV devices.

To measure the electron injection barriers, electroabsorption (EA) spectroscopy was used. Figure 10 (a) shows the EA spectra for the PLED device with Cs_2CO_3 + PPY interlayer.

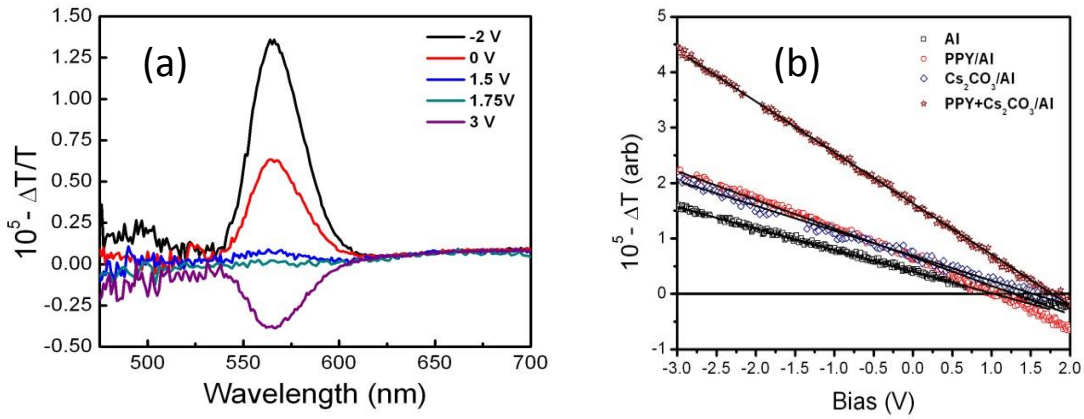

Figure 10. Electroabsorption spectra for the device with structure ITO/PEDOT:PSS(35nm)/MEH-PPV(85nm)/Cs2CO3+PPY(7nm)/Al(100nm) (a) and bias scans for devices with different cathode materials.

There is a strong EA peak at 566 nm which disappears when the V_{DC} applied is 1.75V. It is at this applied external voltage that the built-in potential is cancelled out. Figure 10 (b) shows the bias scans of the EA signal for devices with varying cathode interface layers. The zero-level crossing indicates their built-in potentials. The V_{BI} for the device structure with the Al only cathode is 1.05 V which closely matches the work function difference between Al (4.2 eV) and PEDOT:PSS (5.2 eV). With the addition of PPY, the V_{BI} increases to 1.32v. This can be explained by the formation of an interfacial dipole due to nitrogen donor atom on the side chain of the PPY which lifts the work function of the metal with respect to the LUMO level of the MEH-PPV. When the Cs_2CO_3 + PPY layer is used, the V_{BI} increases to 1.75V from 1.53V when just the Cs_2CO_3 is incorporated. The increase in V_{BI} using PPY clearly shows the barrier for electron injection is lowered yielding better device performance.

4. Publication list

1. R. Casalini, S.W. Tsang, J.J. Deninger, F. A. Arroyave, J.R. Reynolds and F. So, "Investigation of the Role of the Acceptor Molecule in Bulk Heterojunction PV Cells using Impedance Spectroscopy", J. Phys. Chem. C, (2013) dx.doi.org/10.1021/jp401435s
2. Cephas E. Small, Sai-Wing Tsang, Song Chen, Chad M. Amb, Jegadesan Subbiah, John R. Reynolds, Franky So, "Loss Mechanism in Thick-Film Organic Photovoltaic Cell with Low Bandgap Polymer", Advanced Energy Materials, DOI: 10.1002/aenm.201201114(2013).
3. S.W. Tsang, S. Chen and F. So, "Energy Alignment and Sub-bandgap charge generation in polymer:fullerene bulk heterojunction solar cells", accepted for publication, Adv. Mater. adma.201204495. (2013)
4. T.-H. Lai, S.-W. Tsang, J. Manders, S. Chen and F. So "Properties of interlayers for organic Photovoltaics, Materials Today (2013).
5. M. Hartel, S. Chen, B. Swerdlow, HY Hsu, J. Manders, K. Schanze, F. So, "Defect-induced loss mechanisms in polymer-inorganic planar heterojunction solar cells", ACS Appl. Mater. Interfaces, (2013).
6. J.R. Manders, S.W. Tsang, M.J. Hartel, S. Chen, C.A. Amb, J.R. Reynolds, and F. So, " Solution-processed Nickel Oxide Hole Transport Layers in High Efficiency Polymer Photovoltaic Cells", Submitted to *Adv. Funct. Mater.* (2012)
7. M.J. Hartel, J. Subbiah, P.A. Lane, and F. So, "Improvement of polymer light-emitting diodes utilizing a doped polymer interface layer", submitted to *J. Display Technology* Special Issue in Solid State Lighting (2012)
8. C.E. Small, S. Chen, J. Subbiah, C.M. Amb, T.H. Lai, S.W. Tsang, J.R. Reynolds, F. So, "High Efficiency Inverted Dithienogermole-Thienopyrrolodione Based Polymer Solar Cells", *Nature Photonics* 6, 115-120 (2012)
9. S. Chen, C.E. Small, C.A. Amb, J. Subbiah, T.-H. Lai, S.W. Tsang, J. Manders, J.R. Reynolds, and F. So, "High efficiency inverted polymer solar cells with reduced interface recombination", *Adv. Energy Mater*. DOI: 10.1002/aenm.201200184 (2012)
10. S. Chen, J. Manders, S.W. Tsang, J.R. Reynolds, F. So, "Metal-oxides for organic photovoltaics", Invited Progress Report published in *Journal of Materials Chemistry* (2012)
11. C.E. Small, S.W. Tsang, J. Kido, S.K. So, and F. So, "Study of charge injection in inverted organic unipolar devices using n-type hole injection layers", *Adv. Funct. Mater***.** DOI: 10.1002/adfm.201200185 (2012)
12. S. Chen, K. Roy Choudhury, J. Subbiah, C.M. Amb, J.R. Reynolds, and F. So, "Photo-carrier recombination in polymer solar cells based on P3HT and silole-based copolymer", *Adv. Energy Mater*. 1, 963 (2011)
13. Lei Qian, Ying Zheng, Kaushik Roy Choudhury, Debasis Bera, Franky So, Jiangeng Xue, Paul Holloway, "Electroluminescence from light-emitting polymer/ZnO nanoparticle heterojunctions at sub-bandgap voltages", *Nano Today* 5, 384-389 (2010).

References:

1. Qian, L. et al. Electroluminescence from light-emitting polymer/ZnO nanoparticle heterojunctions at sub-bandgap voltages. Nano Today 5, 384-389 (2010).
2. Pandey, A. K. & Nunzi, J. M. Rubrene/fullerene heterostructures with a half-gap electroluminescence threshold and large photovoltage. Adv Mater 19, 3613-+, doi:DOI 10.1002/adma.200701052 (2007).
3. Ng, A. M. C., Djurisic, A. B., Chan, W. K. & Nunzi, J. M. Near infrared emission in rubrene: fullerene heterojunction devices. Chem Phys Lett 474, 141-145, doi:DOI 10.1016/j.cplett.2009.04.024 (2009).
4. Cheng, C. P., Chan, Y. W., Hsueh, C. F. & Pi, T. W. Interfacial electronic properties of the heterojunctions C-60/rubrene/Au and rubrene/C-60/Au. J Appl Phys 112, 023711 (2012).
5. Ryasnyanskiy, A. & Biaggio, I. Triplet exciton dynamics in rubrene single crystals. Phys Rev B 84, doi:Artn 193203 Doi 10.1103/Physrevb.84.193203 (2011).
6. Ma, L. et al. Singlet fission in rubrene single crystal: direct observation by femtosecond pump-probe spectroscopy. Phys Chem Chem Phys 14, 8307-8312, doi:Doi 10.1039/C2cp40449d (2012).
7. Wallikewitz, B. H., Kabra, D., Gelinas, S. & Friend, R. H. Triplet dynamics in fluorescent polymer light-emitting diodes. Phys Rev B 85, doi:Artn 045209 Doi 10.1103/Physrevb.85.045209 (2012).
8. Kondakov, D. Y., Pawlik, T. D., Hatwar, T. K. & Spindler, J. P. Triplet annihilation exceeding spin statistical limit in highly efficient fluorescent organic light-emitting diodes. J Appl Phys 106, doi:Artn 124510 Doi 10.1063/1.3273407 (2009).
9. Zhang, Y. F. & Forrest, S. R. Triplets Contribute to Both an Increase and Loss in Fluorescent Yield in Organic Light Emitting Diodes. Phys Rev Lett 108, doi:Artn 267404 Doi 10.1103/Physrevlett.108.267404 (2012).
10. Tsang, S. W., Chen, S. & So, F. Energy Level Alignment and Sub-Bandgap Charge Generation in Polymer:Fullerene Bulk Heterojunction Solar Cells. Adv Mater 25, 2434-2439, doi:DOI 10.1002/adma.201204495 (2013).